Nano Research

Open Access

Research Article

# Metal doping engineering of $W_{18}O_{49}$ for excellent dual-band electrochromic smart windows with integrated energy storage function

Xiaohui Sun[1,2], Wei Wu[1,2], Xueying Zhao[1,2], Zhaozhu Qu[1,2], Kang Xu[3] ✉, Xuyang Zhang[1,2], Bo Wang[1,2], Xianhui Rong[1,2], Xiangwei Wang[1,2] ✉, Guohua Wu[1,2], and Nana Liu[1,2] ✉

[1] *College of Materials Science and Chemical Engineering, Harbin Engineering University, Harbin 150001, China*
[2] *Qingdao Innovation and Development Center of Harbin Engineering University, Qingdao 266000, China*
[3] *College of Physics and Electronic Information, Dezhou University, Dezhou 253023, China*

**Cite this article:** *Nano Research*, **2025**, *18*, 94907807. https://doi.org/10.26599/NR.2025.94907807

**ABSTRACT:** $W_{18}O_{49}$ is a promising multifunctional material for electrochromic energy storage applications, owing to its abundant oxygen vacancies and distinctive crystalline structure. However, the contradiction between the high transmittance modulation for electrochromism and the high material loading for energy storage severely restricts the development of $W_{18}O_{49}$ in multifunctional smart windows. This work found that different metal doping (Mo, Ti, Fe) exhibited significant differences in regulating the electrochromic performance and energy storage of $W_{18}O_{49}$. And the oxygen vacancies of $W_{18}O_{49}$ can be further controlled by adjusting the metal doping concentration, simultaneously achieving excellent electrochromic properties and energy storage. 5% Ti-doped $W_{18}O_{49}$ not only exhibits a high transmittance modulation of 82.3% (633 nm) and 81.0% (1050 nm) with fast coloration/bleaching times of 9.8/5.8 and 3.8/5.8 s, but also shows a good energy storage of 32.5 mF·cm$^{-2}$ at 0.1 mA·cm$^{-2}$. Theoretical calculations indicate Ti doped $W_{18}O_{49}$ shows a more delocalized characteristic in band decomposition charge densities and a lower diffusion energy barrier, which is conducive to enhancing the electrochemical performance. This work demonstrates metal doping plays a significant role in simultaneously regulating electrochromism and energy storage, providing a new perspective for the development of multifunctional electrochromic materials.

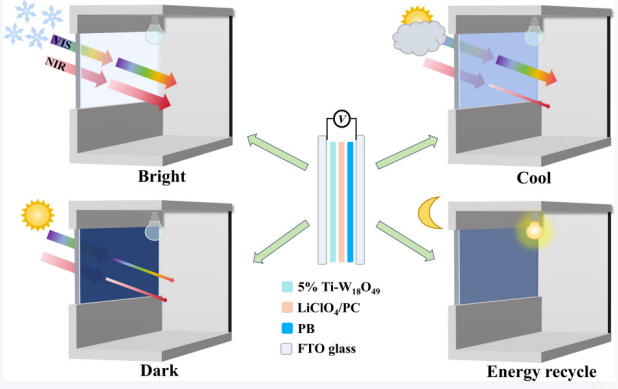


**KEYWORDS:** metal doping, $W_{18}O_{49}$, dual-band, electrochromic, energy storage

## 1 Introduction

Buildings consume over 30% of the global energy and account for 27% of the total $CO_2$ emissions [1–3]. The light and heat carried by sunlight can easily enter the building through the windows and affect the indoor comfort [4–6]. Therefore, the majority of building energy consumption is used to maintain a comfortable indoor environment, such as lighting, cooling, and heating [7]. Electrochromic smart windows (ESW) can dynamically adjust the optical transmittance to reduce the impact of solar energy on the indoor environment [8]. However, near infrared (NIR) light accounts for approximately 43% of the total solar irradiance but contributes nothing to daylighting [9]. The conventional ESW can only control within a wide wavelength, the energy-saving effect is not significant in complex photothermal environments [10]. The dual-band electrochromic smart windows (DESW) can selectively regulate the visible (VIS) and NIR transmittance, and can more effectively reduce building energy consumption in complex thermal and light environments [11, 12].

Dual-band electrochromic materials (DEM) are the most crucial component in DESW [13]. Milliron et al. first prepared a DEM by the localized surface plasmon resonance (LSPR) of indium-tin oxide (ITO) nanocrystals and the polarization mechanism of amorphous $NbO_x$ [14]. However, multicomponent DEM require

**Received:** May 31, 2025; **Revised:** July 12, 2025
**Accepted:** July 15, 2025

✉Address correspondence to Kang Xu, xukang@dzu.edu.cn; Xiangwei Wang, wangxiangwei@hrbeu.edu.cn; Nana Liu, nnliu@hrbeu.edu.cn

different VIS and NIR modulation potentials, as well as excellent film uniformity [15–17]. Obviously, single-component DEM are more favorable for the preparation of the electrochromic films [18, 19]. In recent years, metal-doped $TiO_{2-x}$ [20, 21], $TiO_{2-x}$ [22], and $Nb_2O_{5-x}$ [23] nanocrystals based on the LSPR effect have been successively developed. Unfortunately, these transition metal oxide nanocrystals exhibit relatively low yield and require additional heat treatment to remove the organic ligands [24]. Therefore, the development of a single-component DEM with a simple preparation process and high production efficiency is crucial for the promotion of DESW [25].

Tungsten oxide ($WO_3$) is a promising candidate in single-component DEM due to its optical response ranges being similar to the solar thermal energy distribution [26–28]. However, stoichiometric $WO_3$ has a relatively low free carrier concentration, requiring metal doping or oxygen vacancy self-doping to enhance the LSPR effect [29–31]. $W_{18}O_{49}$ is a non-stoichiometric $WO_3$, featuring abundant oxygen vacancies and a stable crystal structure [32]. The high LSPR of $W_{18}O_{49}$ endows it with excellent NIR absorption capability [33]. $W_{18}O_{49}$ exhibits excellent electrochromic properties through the morphology regulation [34, 35] and crystallinity control [36, 37]. Furthermore, the various crystal cavities of $W_{18}O_{49}$ allow for reversible insertion of ions, making it a multifunctional material for electrochromic energy storage [38, 39]. The DESW integrated with energy storage can reuse the electrical energy consumed during the electrochromic process, thereby further enhancing the energy efficiency of buildings [40]. However, the inherent trade-off between the high transmittance of electrochromism and the high material loading of energy storage remains a major challenge in the $W_{18}O_{49}$-based DESW [41]. How to simultaneously enhance the electrochromic performance and energy storage of materials is a topic worthy of attention.

In this work, metal-doped $W_{18}O_{49}$ films were synthesized through one-step solvothermal method. By controlling the doping metals and the doping concentration, 5% Ti-doped $W_{18}O_{49}$ film simultaneously achieved excellent dual-band electrochromic properties and energy storage. It shows a high transmittance modulation of 82.3% and 81.0% at 633/1050 nm, fast coloration/bleaching times of 9.8/5.8 and 3.8/5.8 s, and coloration efficiency of 34.3/78.3 $cm^2 \cdot C^{-1}$, respectively. And 5% Ti-doped $W_{18}O_{49}$ film simultaneously shows a good energy storag of 32.5 $mF \cdot cm^{-2}$ at 0.1 $mA \cdot cm^{-2}$. Theoretical calculations indicate that the excellent electrochromic energy storage property is attributed to the significant enhancement in the delocalization characteristics of charge density caused by Ti doping, as well as the reduction of the diffusion energy barrier of Li ions. The simple metal doping engineering provides a new idea for the development of high-performance electrochromic energy storage materials.

## 2 Experimental

### 2.1 Chemical reagent

$WCl_6$ (99.9%), $TiCl_4$ (99.9%), $MoCl_5$ (99.6%), $FeCl_3$ (99.9%), $K_3[Fe(CN)_6]$ (99.5%), KCl (99%), and propylene carbonate (PC, 99%) were purchased from Aladdin Biochemical Technology Co., Ltd. Fluorine-doped tin oxide glass (FTO, 2.5 × 5 $cm^{-2}$, 8 $\Omega \cdot sq^{-1}$) was purchased from Zhuhai Kaivo Optoelectronic Technology Co., Ltd. $LiClO_4$ (99.9%) and ethanol (99.8%) were purchased from Sinopharm Chemical Reagent Co., Ltd. All reagents were not further purified.

### 2.2 Synthesis of $W_{18}O_{49}$ and metal-doped $W_{18}O_{49}$ films

The preparation process of the electrochromic film is shown in Fig. 1. 396.6 mg (1 mmol) $WCl_6$ was added to 30 mL ethanol and stirred for 10 min to form a homogeneous precursor solution. The FTO glass with the conductive surface facing down was placed inside a 100 mL Teflon-lined autoclave, and the precursor solution was added and heated to 180 °C for 12 h. After the solvothermal reaction was completed, the autoclave naturally cooled to room temperature. Finally, the $W_{18}O_{49}$ film grown on the FTO glass was cleaned with ethanol and then naturally dried. The preparation process of metal-doped $W_{18}O_{49}$ films is like that of $W_{18}O_{49}$, except that different molar doping amounts of $TiCl_4$ (3%, 5%, 7%), $MoCl_5$ (5%), and $FeCl_3$ (5%) are added in the precursor solution. According to the doping concentration and metal, the prepared films are respectively named as 3% Ti-$W_{18}O_{49}$, 5% Ti-$W_{18}O_{49}$, 7% Ti-$W_{18}O_{49}$, 5% Mo-$W_{18}O_{49}$, and 5% Fe-$W_{18}O_{49}$.

### 2.3 Assembly of electrochromic device

A 5% Ti-$W_{18}O_{49}$ film was used as the negative electrode, and a Prussian blue (PB) film as the positive electrode. The preparation method of PB film is the same as our previous paper [35]. 1 M $LiClO_4$/PC was used as the electrolyte. 3M tape was used as the interlayer between the electrodes, and the device were sealed with UV-curable glue.

### 2.4 Instruments and characterization

The X-ray diffraction (XRD) was characterized by Bruker D8 Advance. The X-ray photoelectron spectroscopy (XPS) was analyzed by Thermo Fisher Scientific K-Alpha. The electron paramagnetic resonance (EPR, Bruker EMX plus) was employed to

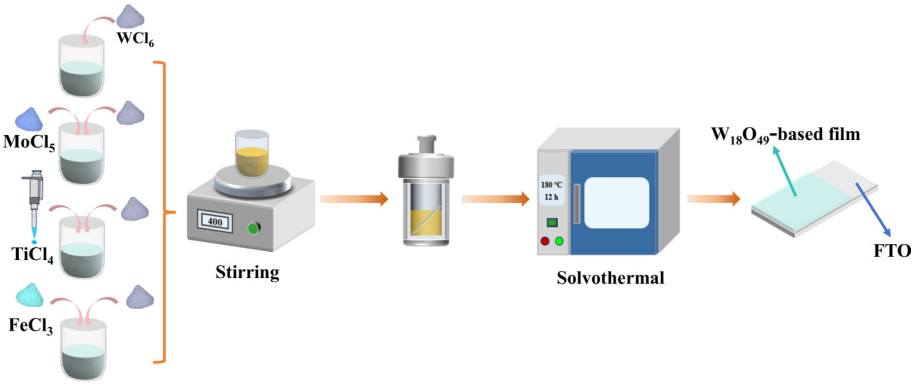


**Figure 1** Schematic illustration of preparing films.

characterize oxygen vacancies. The scanning electron microscope (SEM, Zeiss Sigma 300) was used to observe the morphology structures. The element mapping was achieved through energy dispersive X-ray spectroscopy (EDS). The transmission electron microscopy (TEM, Hitachi JEM 2100F) was used to observe the microstructure. The high-resolution lattice spacing of the material is characterized by high angle angular dark field-scanning transmission electron microscopy (HADDF-STEM). The electrochemical and electrochromic performance of the films were carried out by electrochemical workstation (CHI 660E) and optical fiber spectrometer (Avaspec-ULS2048CL-EVO). In the three-electrode system, the electrochromic film, Pt electrode and Ag/AgCl are respectively used as the working electrode, the counter electrode and reference electrode.

### 2.5 Theoretical calculations

All calculations were carried out by the first principle electronic structure software-the Vienna *ab initio* simulation package (VASP) [42, 43]. The Perdew–Burke–Ernzerhof (PBE) functional using the generalized gradient approximating was adopted to describe the electron exchange and correction [44]. The projector augmented wave (PAW) method together with plane wave basis sets were used to describe valance electron states [45]. W 6s5d, O 2s2p, Mo 4s4d, Fe 4s3d, Ti 4s3d, Li 1s electrons are treated as valence electrons in the PAW potentials. The energy cutoff of plane wave basis set is 450 eV. For electronic structure calculations and climbing image nudged elastic band (CI-NEB) calculations, a 1 × 2 × 1 supercell containing one oxygen vacancy with or without two transition metal atoms were used. All atoms were fully relaxed during structural relaxation until the atomic forces were smaller than 0.01 eV·Å$^{-1}$ on each atom site. Monkhorst-Pack k-points mesh of 1 × 2 × 1 was employed for all calculations. The CI-NEB method was used to calculate the diffusion barriers, the force accuracy of –0.03 eV·Å$^{-1}$ was employed [46].

## 3 Results and discussion

The XRD patterns (Fig. 2(a)) exhibit characteristic peaks of monoclinic $W_{18}O_{49}$ (JCPDF 71-2450), where the prominent peaks at 23.3° and 47.4° correspond to the (010) and (020) crystal planes, respectively [16]. The (010) peak of Ti-$W_{18}O_{49}$ shifts to 23.2° (3% Ti), 23.1° (5% Ti), and 23.1° (7% Ti) with the increase of Ti doping. Similarly, the XRD patterns of 5% Mo-$W_{18}O_{49}$ (Fig. S1(a) in the Electronic Supplementary Material (ESM)) and 5% Fe-$W_{18}O_{49}$ (Fig. S1(d) in the ESM) only show the diffraction peaks of $W_{18}O_{49}$, with the (010) diffraction peaks located at 23.2° and 23.1°, respectively. The (010) diffraction peak of metal-doped $W_{18}O_{49}$ shifts to a lower angle, indicating that the metal doping slightly increases the lattice spacing of (010). The XRD of metal-doped $W_{18}O_{49}$ shows no diffraction peaks of other metal oxides, indicating that the metal elements have been successfully doped into $W_{18}O_{49}$. The elemental composition and chemical states of the materials were further characterized using XPS. The XPS surveys of $W_{18}O_{49}$ and Ti-$W_{18}O_{49}$ (Fig. 2(b)) confirmed the presence of W and O elements. The Ti 2p characteristic peaks of Ti-$W_{18}O_{49}$ gradually intensified with the increasing Ti doping content, which is consistent with the high-resolution fitting results of Ti 2p (Figs. 2(c)–2(e)). And the high-resolution XPS of Mo-$W_{18}O_{49}$ and Fe-$W_{18}O_{49}$ also revealed

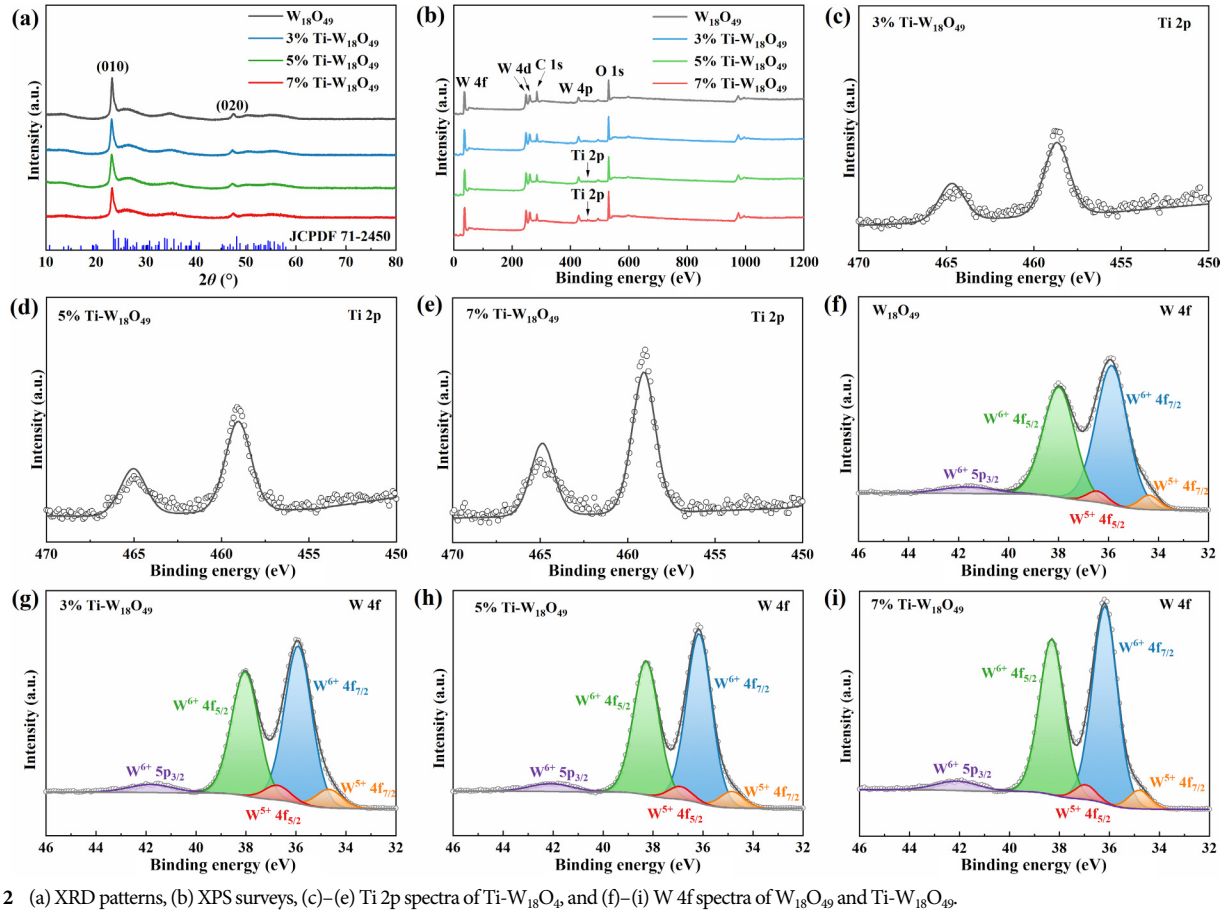


**Figure 2** (a) XRD patterns, (b) XPS surveys, (c)–(e) Ti 2p spectra of Ti-$W_{18}O_4$, and (f)–(i) W 4f spectra of $W_{18}O_{49}$ and Ti-$W_{18}O_{49}$.

the fitted peaks of Mo 3d (Fig. S1(b) in the ESM) and Fe 2p (Fig. S1(e) in the ESM), suggesting that the metal elements were successfully doped into $W_{18}O_{49}$. The deconvoluted triplet peaks of W 4f (Figs. 2(f)–2(i)) are identified as $W^{6+}$ $4f_{7/2}$, $W^{6+}$ $4f_{5/2}$, and $W^{6+}$ $5p_{3/2}$, indicating a the hybrid electronic structure [11]. The $W^{5+}$ area ratio of Ti-$W_{18}O_{49}$ is higher than that of $W_{18}O_{49}$, suggesting Ti doping increases the concentration of oxygen vacancies through the charge compensation mechanism [47]. A symmetric EPR signal ($g$ = 2.0038) of Fig. S2 in the ESM is characteristic of unpaired electrons trapped in oxygen defects [27]. 5% Ti-$W_{18}O_{49}$ exhibits higher EPR peak, indicating that Ti doping does indeed increase the oxygen vacancies of $W_{18}O_{49}$. From the W 4f spectra of 5% Mo-$W_{18}O_{49}$ (Fig. S1(c) in the ESM) and 5% Fe-$W_{18}O_{49}$ (Fig. S1(f) in the ESM), it can be seen that Mo doping reduces the oxygen vacancy concentration, while Fe doping increases it. An appropriate oxygen vacancy concentration can enhance the electrochromic performance [36, 48].

The morphology images of the $W_{18}O_{49}$ and metal-doped $W_{18}O_{49}$ films were characterized by SEM. $W_{18}O_{49}$ film (Figs. 3(a) and 3(b)), Ti-$W_{18}O_{49}$ (Figs. 3(c)–3(h)), Mo-$W_{18}O_{49}$ (Figs. S3(a) and S3(b) in the ESM), and Fe-$W_{18}O_{49}$ (Figs. S3(d) and S3(e) in the ESM) films are all similar porous nanowire structure. Compared with Ti-$W_{18}O_{49}$ and Mo-$W_{18}O_{49}$ nanowires, $W_{18}O_{49}$ and Fe-$W_{18}O_{49}$ nanowires exhibit slightly smaller diameters. The EDS mappings (Figs. 3(i)–3(l), and Figs. S3(c) and S3(f) in the ESM) reveal a uniform distribution of doped metals (Ti, Mo, and Fe), W, and O, indicating that the metal elements have been successfully uniformly doped into $W_{18}O_{49}$. In Figs. 4(a) and 4(d), and Figs. S4(a) and S5(a) in the ESM, the TEM images of $W_{18}O_{49}$ and metal-doped $W_{18}O_{49}$ show the same nanowire structure as that observed in SEM. The interplanar spacing of $W_{18}O_{49}$ was further determined to be 0.382 nm by HAADF-STEM (Figs. 4(b) and 4(c)), which corresponds to the (010) crystal plane of $W_{18}O_{49}$ [11]. This observation is consistent with the preferred orientation revealed in the XRD characterization. Due to the similar ionic diameters of the doped metals to that of W, the (010) interplanar spacings of 5% Ti-$W_{18}O_{49}$ (Figs. 4(e) and 4(f)), 5% Mo-$W_{18}O_{49}$ (Fig. S4(b) in the ESM) and 5% Fe-$W_{18}O_{49}$ (Fig. S5(b) in the ESM) are 0.383, 0.381, and 0.385 nm, respectively. And EDS mapping of nanowire reveals the uniform doping of Ti (Figs. 4(g)–4(j)), Mo (Figs. S4(c)–S4(f) in the ESM), and Fe (Figs. S5(c)–S5(f) in the ESM) into the $W_{18}O_{49}$. Metal doping engineering with atomic-scale compatibility enables $W_{18}O_{49}$ to maintain structural stability while achieving tailored properties [49, 50].

To investigate the effect of metal doping on the transmittance of $W_{18}O_{49}$, the transmittance modulation ($\Delta T$) is calculated by using Eq. (1)

$$\Delta T = T_b - T_c \quad (1)$$

where $T_b$ is the transmittance of bleached sate and $T_c$ is the transmittance of coloration sate. As shown in Fig. S7(a) in the ESM, $W_{18}O_{49}$ film shows a $\Delta T$ of 70.3% at 633 nm and 71.1% at 1050 nm. Ti doping enhances the NIR transmittance of $W_{18}O_{49}$ in the bleached state while reducing the VIS and NIR transmittance in the coloration state (Fig. 5(a)), thereby simultaneously improving both the VIS and NIR $\Delta T$ of $W_{18}O_{49}$. As can be seen from Fig. 5, and Figs. S8 and S9 in the ESM, the electrochromic performance of the 5% Ti-$W_{18}O_{49}$ is superior to that of the 3% Ti-$W_{18}O_{49}$ and 7% Ti-$W_{18}O_{49}$. The 5% Ti-$W_{18}O_{49}$ film achieves a remarkable $\Delta T$ of 82.3% at 633 nm and 81.0% at 1050 nm. The 5% Ti-$W_{18}O_{49}$ film exhibits voltage-dependent tunable transmittance (Fig. 5(b)), enabling various transmittance modes including bright, cold, and dark modes. And it shows reversible switching between transparent and deep blue (Fig. 5(c)) with different applied potentials. In Fig. S6(a) in the ESM, Mo doping also enhances the $\Delta T$ of $W_{18}O_{49}$, 5% Mo-$W_{18}O_{49}$ film shows a $\Delta T$ of 81.9%/77.5% at 633/1050 nm, respectively. While Fe doping has almost no effect on the $\Delta T$ of $W_{18}O_{49}$ (72.8%/71.9% at 633/1050 nm). Response time is the time corresponding to the 90% $\Delta T$ of reaching the bleached ($t_b$) and coloration ($t_c$) states, suggesting the speed of electrochromic modulation. The $W_{18}O_{49}$ film exhibits a good $t_c/t_b$ of 10.3/3.0 s at 633 nm (Fig. S7(b) in the ESM) and 4.7/5.5 s at 1050 nm (Fig. S7(c) in the ESM). When 5% Ti-$W_{18}O_{49}$ shows an increased $\Delta T$, $t_c$ is faster than $W_{18}O_{49}$, while $t_b$ only increases slightly. 5% Ti-$W_{18}O_{49}$

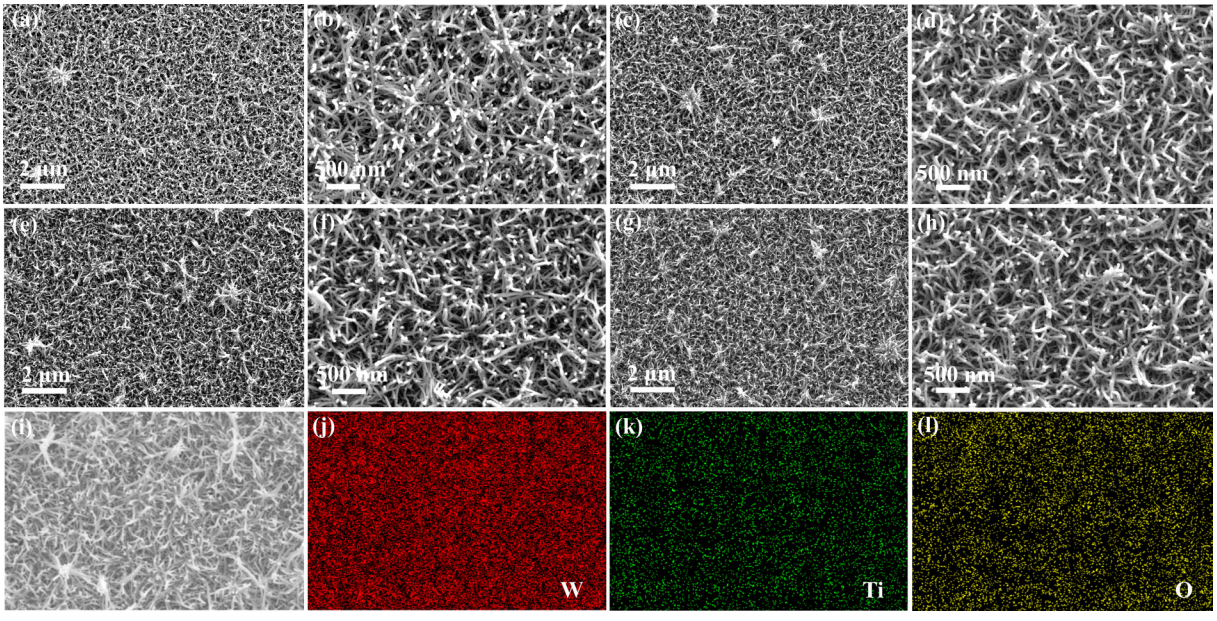


**Figure 3** SEM images of ((a) and (b)) $W_{18}O_{49}$ film, ((c) and (d)) 3% Ti-$W_{18}O_{49}$ film, ((e) and (f)) 5% Ti-$W_{18}O_{49}$ film, and ((g) and (h)) 7% Ti-$W_{18}O_{49}$ film. (i)–(l) EDS mappings of 5% Ti-$W_{18}O_{49}$ film.

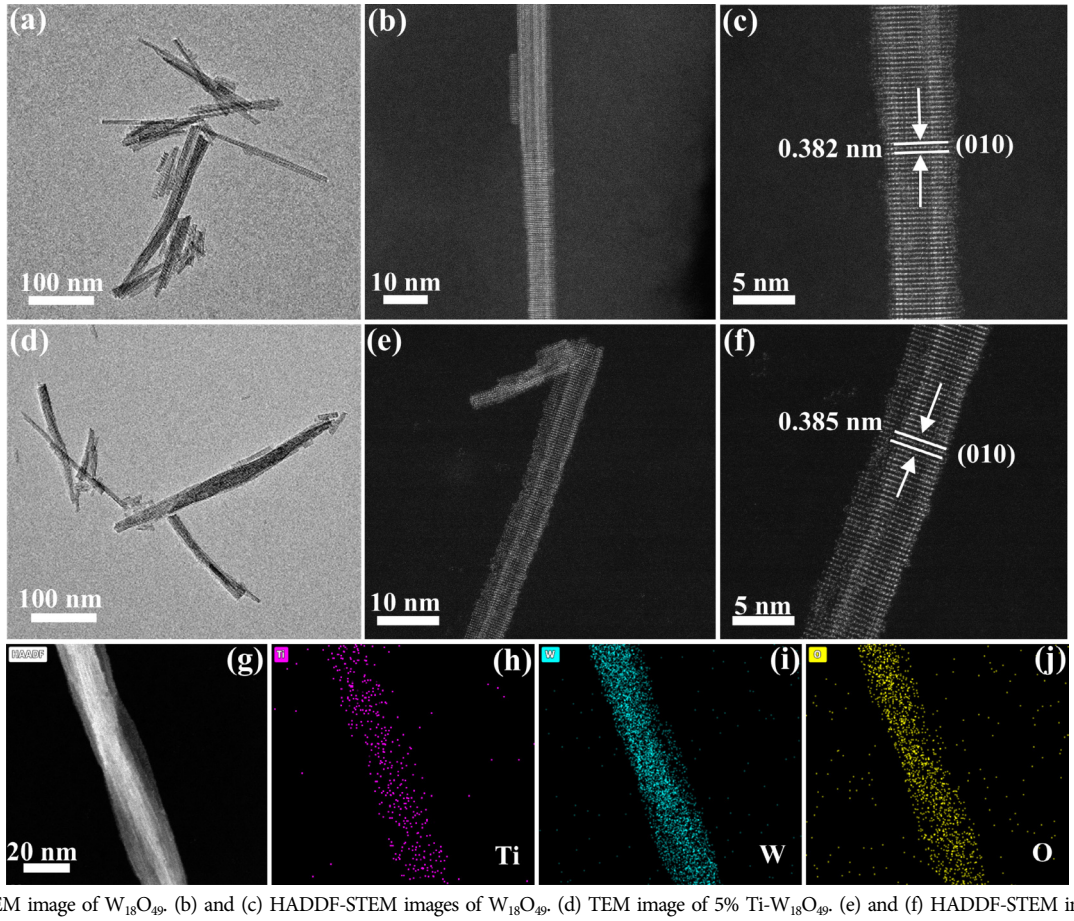


**Figure 4** (a) TEM image of $W_{18}O_{49}$. (b) and (c) HADDF-STEM images of $W_{18}O_{49}$. (d) TEM image of 5% Ti-$W_{18}O_{49}$. (e) and (f) HADDF-STEM images of 5% Ti-$W_{18}O_{49}$. (g)–(j) EDS mappings of 5% Ti-$W_{18}O_{49}$ nanowire.

still exhibits a fast $t_c/t_b$ of 9.8/5.8 s at 633 nm (Fig. 5(d)) and 3.8/5.8 s at 1050 nm (Fig. 5(e)). Instead, the $t_c/t_b$ (11.1/10.6 s at 633 nm, 5.1/11.2 s at 1050 nm) of 5% Mo-$W_{18}O_{49}$ is significantly slower than that of $W_{18}O_{49}$, as shown in Figs. S10(b) and S10(c) in the ESM. However, 5% Fe-$W_{18}O_{49}$ exhibits a faster $t_c/t_b$ (8.6/2.7 s at 633 nm, 5.1/2.9 s at 1050 nm) in Figs. S11(b) and S11(c) in the ESM. The response time is related to the electrochemical impedance spectroscopy. The charge transfer resistance ($R_{CT}$) and diffusion rate of the film were analyzed through Nyquist plots. The diameter of the semicircle in the high-frequency region represents the $R_{CT}$, while the slope of the straight line in the low-frequency region represents the ion diffusion [38]. In Fig. S12 in the ESM, Ti and Fe increases doping can reduce the $R_{CT}$ of $W_{18}O_{49}$, while Mo doping not only the $R_{CT}$ but also reduces the ion diffusion, which is similar to the change of response time. A high coloration efficiency (CE) indicates that achieving the same $\Delta T$ requires less energy consumption, Eq. (2) is as follows

$$CE = \frac{\Delta OD}{\Delta Q} = \frac{\lg \frac{T_b}{T_c}}{\Delta Q} \quad (2)$$

where ΔOD is the change of optical density at the specified wavelength, $\Delta Q$ is injected charge density ($C \cdot cm^{-2}$) at the corresponding $T_c$. In Fig. 5(f), the CE of 5% Ti-$W_{18}O_{49}$ is 34.3/78.3 $cm^2 \cdot C^{-1}$ (633/1050 nm), which is superior to 30.2/54.5 $cm^2 \cdot C^{-1}$ of $W_{18}O_{49}$ (Fig. S7(d) in the ESM), 32.4/60.5 $cm^2 \cdot C^{-1}$ of 5% Mo-$W_{18}O_{49}$ (Fig. S10(d) in the ESM), and 36.7/60.2 $cm^2 \cdot C^{-1}$ of 5% Fe-$W_{18}O_{49}$ (Fig. S11(d) in the ESM). Cycle stability is importance in practical application, the $\Delta T$ of $W_{18}O_{49}$ exhibits significant degradation during long-term cycle (Figs. S7(g)–S7(i) in the ESM). In Figs. 5(g)–5(i), and Figs. S10(g)–S10(i) and S11(g)–S11(i) in the ESM, metal doping can enhance the electrochromic stability. And 5% Ti-$W_{18}O_{49}$ still maintains a high $\Delta T$ of 80.5% (633 nm) and 79.5% (1050 nm) even after 6000 s. The above results indicate that different metal doping leads to significant differences in the electrochromic performance of $W_{18}O_{49}$, making it essential to rationally select metal doping elements.

The effects of metal doping on electrochemical performance were further investigated. The galvanostatic charge–discharge (GCD) curves of $W_{18}O_{49}$ and Ti-$W_{18}O_{49}$ are shown in Fig. 6(a), 5% Ti-$W_{18}O_{49}$ shows the longest discharge time. And the GCD (Fig. 6(b)) of 5% Ti-$W_{18}O_{49}$ exhibits good symmetry at different current densities, indicating an excellent reversible electrochemical energy storage. The areal specific capacity ($C_s$) is calculated by the following Eq. (3)

$$C_s = \frac{It}{A\Delta V} \quad (3)$$

where $I$ (A) is the discharge current, $t$ (s) is the discharge time, $A$ ($cm^2$) is the effective area of the electrode, $\Delta V$ (V) is the potential window. As shown in Table S1 in the ESM, previous studies have either neglected the energy storage of $W_{18}O_{49}$ films, or adopted the strategy of compositing $W_{18}O_{49}$ with other materials to improve energy storage capacity at the expense of reduced $\Delta T$. Compare to $W_{18}O_{49}$ (25.7 $mF \cdot cm^{-2}$), 5% Ti-$W_{18}O_{49}$ achieves an excellent $C_s$ of 32.5 $mF \cdot cm^{-2}$ at 0.1 $mA \cdot cm^{-2}$ (Fig. 6(c)) and a high $\Delta T$. In Fig. S6(b)

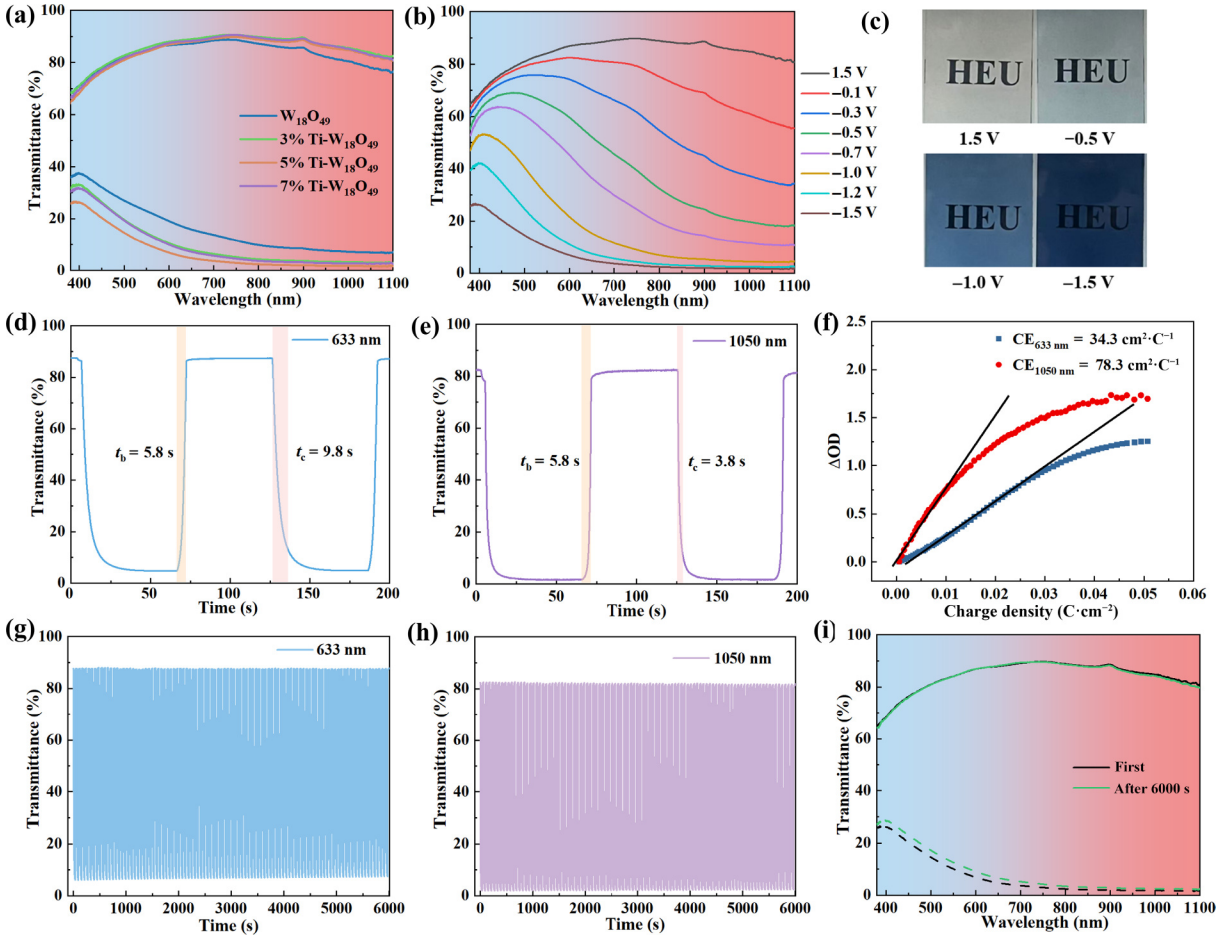


**Figure 5** (a) Transmittance spectra of $W_{18}O_{49}$ and Ti-$W_{18}O_{49}$. Electrochromic properties of 5% Ti-$W_{18}O_{49}$: (b) transmittance modulation, (c) digital photographs at different voltages, (d) and (e) response time, (f) CE, (g) and (h) electrochromic switching stability, and (i) transmittance spectra after 100 cycles.

in the ESM, the discharge time of 5% Mo-$W_{18}O_{49}$ is longer than that of 5% Ti-$W_{18}O_{49}$ and 5% Fe-$W_{18}O_{49}$. As shown in Fig. S6(c) in the ESM, the $C_s$ of 5% Mo-$W_{18}O_{49}$ can reach 32.7 mF·cm$^{-2}$, while that of 5% Fe-$W_{18}O_{49}$ is only 18.2 mF·cm$^{-2}$. However, 5% Mo-$W_{18}O_{49}$ degrades dramatically to 12.9 mF·cm$^{-2}$ at 1.0 mA·cm$^{-2}$. The 5% Ti-$W_{18}O_{49}$ film still maintained 15.6 mF·cm$^{-2}$ at 1.0 mA·cm$^{-2}$, demonstrating superior rate capability. The transmittance of 5% Ti-$W_{18}O_{49}$ can be controlled through adjusting the charge–discharge potential, the $\Delta T$ of 633 nm (Fig. 6(d)) and 1050 nm (Fig. 6(e)) can reach 76.1% and 75.9%, respectively. The 5% Ti-$W_{18}O_{49}$ film exhibits a significantly larger cyclic voltammetry (CV) area (Fig. 6(f)) compared to the 3% Ti-$W_{18}O_{49}$, 7% Ti-$W_{18}O_{49}$ and $W_{18}O_{49}$. 5% Ti-$W_{18}O_{49}$ and 5% Mo-$W_{18}O_{49}$ exhibit a larger CV area than 5% Fe-$W_{18}O_{49}$ in Fig. S6(d) in the ESM, which is similar to the GCD results. Overall, 5% Ti-$W_{18}O_{49}$ exhibits significantly better electrochromic energy storage. The charge storage mechanism can be analyzed through CV curves (Fig. 6(g)), as shown in Eqs. (4) and (5) [51]

$$I_p = av^b \tag{4}$$

$$\lg(I_p) = \lg(a) + b\lg(v) \tag{5}$$

where $I_p$ (A) is the peak current of CV curve, $a$ and $b$ are fitted parameter, $v$ is the scan rate (V·s$^{-1}$). Ion diffusion plays a predominant role in charge storage as the $b$ value approaches 0.5, whereas surface capacitance becomes the primary contributor when the $b$ value tends towards 1 [51]. In Fig. 6(h), the fitted $b$ values are 0.66 and 0.58 respectively, indicating that the electrochemical process of 5% Ti-$W_{18}O_{49}$ film is mainly controlled by diffusion. And the contribution ratios of surface capacitance and diffusion can be further calculated using Eqs. (6) and (7) [17]

$$I_p = k_1 v + k_2 v^{1/2} \tag{6}$$

$$I_p / \left(v^{1/2}\right) = k_1 v^{1/2} + k_2 \tag{7}$$

where $I_p$ is the peak current (A), $k_1$ and $k_2$ are fitted parameter, $v$ is the scan rate (V·s$^{-1}$). In Fig. 6(i), the diffusion contribution is 55.6% at 5 mV·s$^{-1}$, ion diffusion plays a dominant role. As the scan rate increases, the contribution ratio of surface capacitance gradually increases, accounting for 97.2% at 100 mV·s$^{-1}$. The ratio of the current to the square root of the scan rate is shown in Fig. S13 in the ESM, the Ti doping significantly enhances the ion diffusion of $W_{18}O_{49}$, which is beneficial for achieving excellent electrochromic energy storage. The $Li^+$ mobility can be calculated based on the Randles Sevcik equation (Eq. (8)) [38]

$$I_p = 2.69 \times 10^5 \times n^{2/3} \times A \times D^{1/2} \times C_0 \times v^{1/2} \tag{8}$$

where $I_p$ represents the peak current (A) of the CV, $n$ is the electron transfer number, $A$ is the working electrode area (cm$^2$), $D$ (cm$^2$·s$^{-1}$)

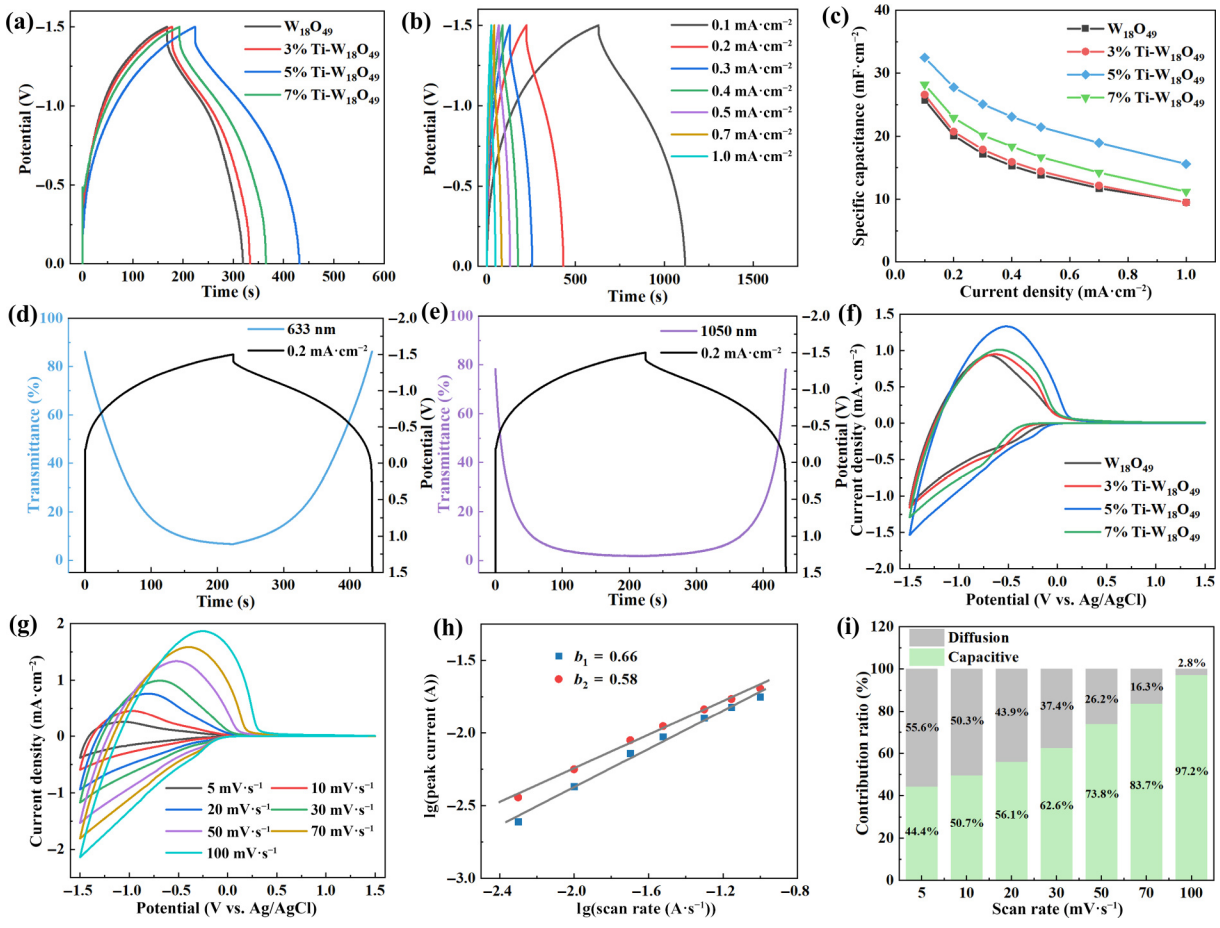


**Figure 6** (a) GCD curves at 0.2 mA·cm$^{-2}$. (b) GCD of 5% Ti-$W_{18}O_{49}$ film. (c) Areal specific capacitance. (d) and (e) Transmittance change at 0.2 mA·cm$^{-2}$. (f) CV at 50 mV·s$^{-1}$. (g) CV of 5% Ti-$W_{18}O_{49}$ film. (h) The logarithmic relationship between scan rate and peak current. (i) The contribution ratio of energy storage.

indicates the diffusion coefficient, $C_0$ is the active ion concentration (mol·cm$^{-3}$), $v$ is the scan rate (V·s$^{-1}$). The $Li^+$ mobility (reduction reaction) of 5% Ti-$W_{18}O_{49}$ is the highest ($6.08 \times 10^{-10}$ cm$^2$·s$^{-1}$), significantly superior to $2.83 \times 10^{-10}$ cm$^2$·s$^{-1}$ of $W_{18}O_{49}$, $3.83 \times 10^{-10}$ cm$^2$·s$^{-1}$ of 5% Mo-$W_{18}O_{49}$, and $8.82 \times 10^{-11}$ cm$^2$·s$^{-1}$ of 5% Fe-$W_{18}O_{49}$, respectively.

First-principles calculations were employed to elucidate the mechanisms by which oxygen vacancy self-doping and metal doping affect the electrochemical reaction. Figure S14 in the ESM shows the doped crystal model, which are constructed along the preferred orientation (010) crystal plane of $W_{18}O_{49}$. From the density of states (DOS) of W and O atoms in Fig. 7(a), it can be seen that the O-p state mainly contributes to the valence band region, while the W-d state mainly contributes to the conduction band region. It can also be found that defect states mainly composed of W 5d electrons are generated in the bandgap of these doped crystal structures, which is very favorable for electron transport. To investigate the effect of doping on the charge DOS, the band decomposition charge densities were constructed (Figs. 7(b)–7(e)), the isosurface of the charge density corresponds to 0.0008 e·Å$^{-1}$. Compared with oxygen vacancy self-doping, Mo doping and Fe doping; the defect states of Ti-doped structure show a more delocalized characteristic, suggesting Ti-$W_{18}O_{49}$ has a better conductivity [52]. In addition, the diffusion energy barrier of Ti-$W_{18}O_{49}$ is 0.59 eV, which is lower than that of other doped $W_{18}O_{49}$, as shown in Figs. 7(f)–7(i). These theoretical calculations suggest that Ti doping is more effective in enhancing the electrochemical reaction of $W_{18}O_{49}$, thereby simultaneously achieving excellent electrochromism and energy storage [27]. The analysis results indicates that the Ti doping promotes the diffusion kinetics of $W_{18}O_{49}$.

PB is an anodic electrochromic material, which can complement the optical modulation of $WO_3$-based devices [53, 54]. Therefore, PB is used as the counter electrode of Ti-$W_{18}O_{49}$, the schematic diagram of the device structure is shown in Fig. 8(a). The 5% Ti-$W_{18}O_{49}$ device can reach a $\Delta T$ of 63.2% at 633 nm and 60.5% at 1050 nm (Fig. 8(b)). And the transmittance can be adjusted by the applied voltage to achieve the bright, cool, and dark modes. The device also shows a fast $t_c/t_b$ (Fig. 8(c)) of 2.3/5.8 s (633 nm) and 2.7/9.8 s (1050 nm), as well as a high CE (Fig. 8(d)) of 89.3/97.8 cm$^2$·C$^{-1}$ at 633/1050 nm. The error bars of the device performance maintained good stability (Fig. S15 in the ESM). The device can maintain a coloration transmittance of 94.9% (633 nm) and 95.5% (1050 nm) after 3600 s (Fig. 8(e)), as well as a bleached transmittance of 84.3% (633 nm) and 88.3% (1050 nm). The device shows excellent stability after 6000 s of long-term cycle (Fig. 8(f)), the $\Delta T$ still reaches 61.3% (633 nm) and 58.3% (1050 nm). The device was placed at 60 °C for 12 h to test the heat resistance. Compared with the fresh device, the NIR transmittance of the device shows no significant change after high-temperature treatment, as shown in Fig. S16 in the ESM. It still exhibits the $\Delta T$ of 59.2% at 1050 nm. Meanwhile, the transmittance of bleached state shows a slightly decreased in the VIS range, with a $\Delta T$ of 58.4% at 633 nm. The device also exhibits a good energy storage of

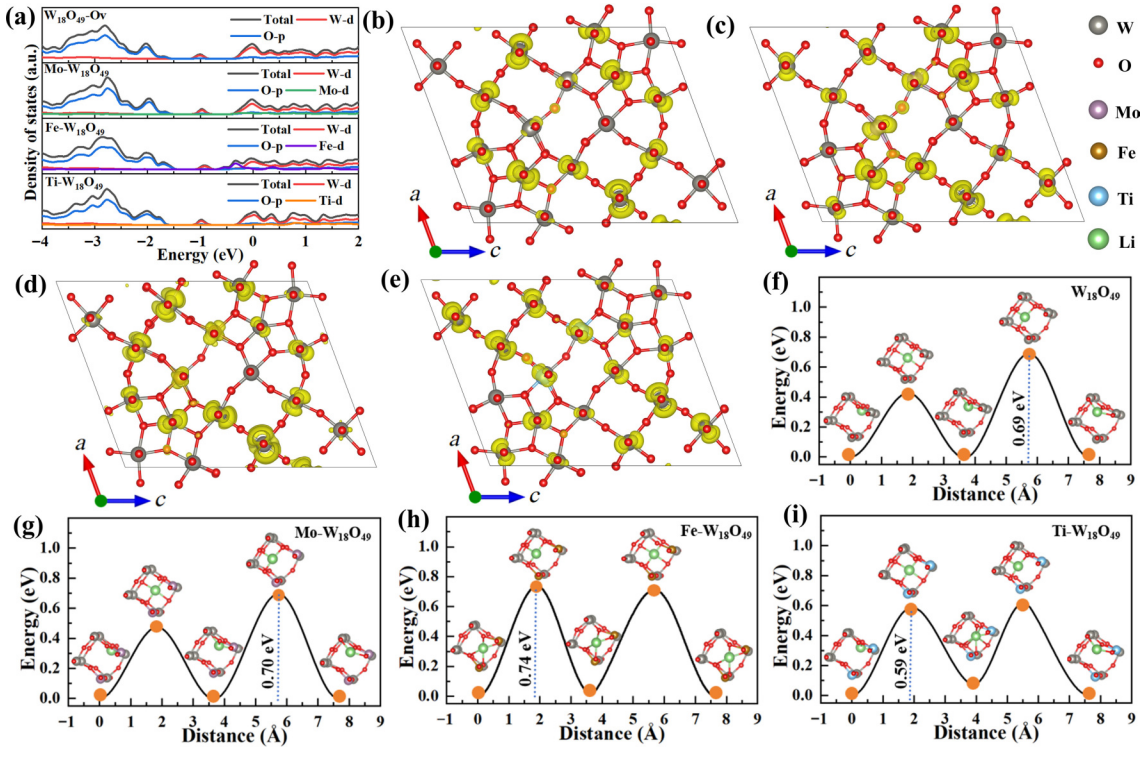


**Figure 7** (a) Density of states. Band decomposed charge density of defect states: (b) oxygen-vacancy $W_{18}O_{49}$, (c) Mo-$W_{18}O_{49}$, (d) Fe-$W_{18}O_{49}$, and (e) Ti-$W_{18}O_{49}$. The $Li^+$ diffusion energy barrier of (f) oxygen-vacancy $W_{18}O_{49}$, (g) Mo-$W_{18}O_{49}$, (h) Fe-$W_{18}O_{49}$, and (i) Ti-$W_{18}O_{49}$.

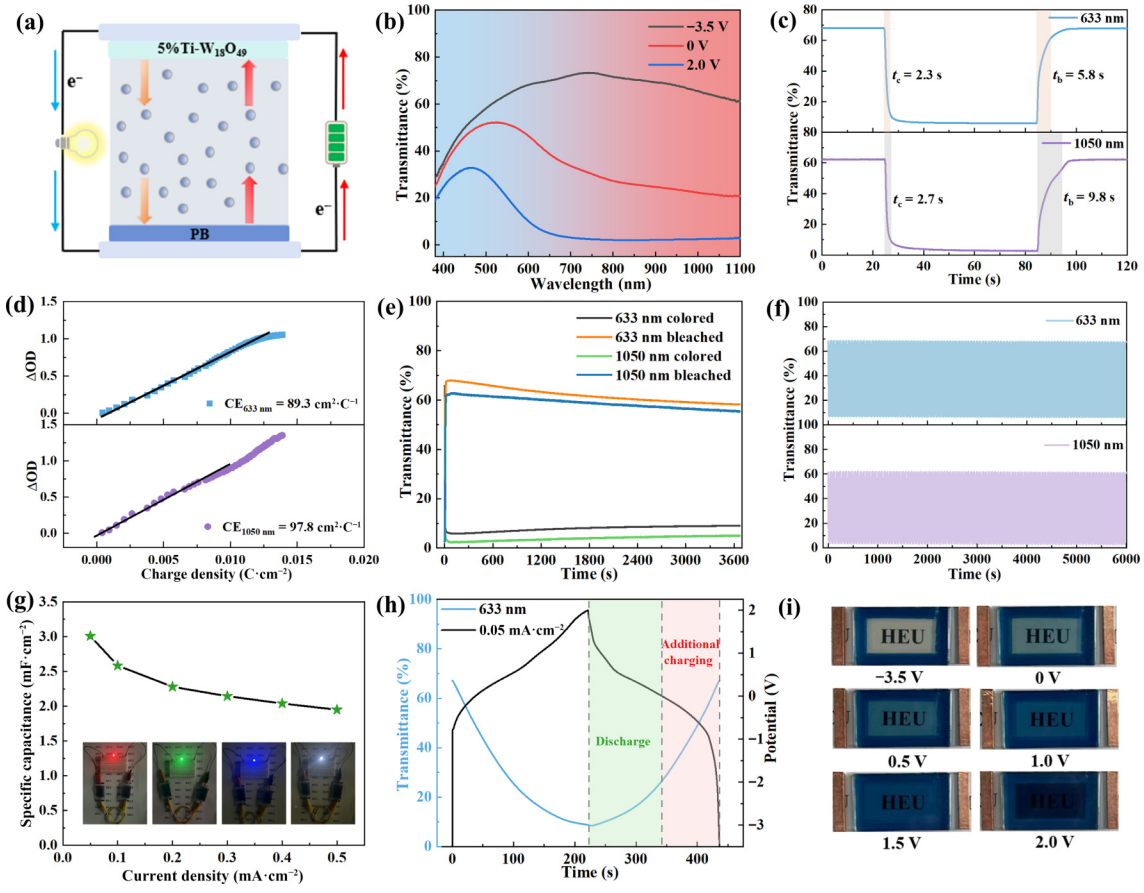


**Figure 8** (a) 5% Ti-$W_{18}O_{49}$ device, (b) transmittance spectra, (c) response time, (d) CE, (e) device state stability, (f) electrochromic stability, (g) areal specific capacitance (inset photos show that two devices connected in series to light up different colored LED bulbs), (h) transmittance change at 0.05 $mA \cdot cm^{-2}$, and (i) digital photographs at different applied voltages.

3.01 mF·cm$^{-2}$ at 0.05 mA·cm$^{-2}$ (Fig. 8(g)), and it still maintains 1.95 mF·cm$^{-2}$ at 0.5 mA·cm$^{-2}$. Two devices connected in series can power different-colored light-emitting device (LED) bulbs, demonstrating their potential in energy recycling. As shown in Fig. 8(h), the device has been completely discharged at 0.05 mA·cm$^{-2}$, it cannot fully return to the initial transmittance. And an additional 1.34 mF·cm$^{-2}$ of electrical energy is still required. The DESW with integrated energy storage can recover 69.2% of the energy, significantly improving the energy efficiency of the device. And the color state of the device (Fig. 8(i)) can be used to determine the potential level. Although the energy storage capacity of the 5% Ti-$W_{18}O_{49}$ device is relatively low, if DESW integrated energy storage are widely adopted on a large scale, the total energy savings will be considerable.

## 4 Conclusion

In summary, we synthesized metal-doped $W_{18}O_{49}$ films by one-step solvothermal method. It was found that different metal doping elements exhibit significant differences in regulating the electrochromic energy storage of $W_{18}O_{49}$. In particular, Ti doping can simultaneously enhance both electrochromism and energy storage. Moreover, the oxygen vacancies of $W_{18}O_{49}$ can be precisely controlled by adjusting the Ti doping concentration. The 5% Ti-$W_{18}O_{49}$ film shows a high $\Delta T$ of 82.3% (633 nm) and 81.0% (1050 nm), while still maintaining good energy storage of 32.5 mF·cm$^{-2}$ at 0.1 mA·cm$^{-2}$. The theoretical calculations also demonstrate that Ti doping can better enhance the delocalization characteristics of $W_{18}O_{49}$ in charge density and reduce the diffusion energy barrier of Li ions. And the 5% Ti-$W_{18}O_{49}$ device still shows a high $\Delta T$ of 63.2% (633 nm) and 60.5% (1050 nm) with 3.02 mF·cm$^{-2}$ at 0.05 mA·cm$^{-2}$. This work demonstrates that the selection of metal doping elements in doping engineering is of great significance, which provides new insights for the development of high-performance multifunctional devices.

**Electronic Supplementary Material**: Supplementary material (the XRD patterns, XPS spectra, SEM and TEM images, electrochromic and electrochemical properties of 5% Mo-$W_{18}O_{49}$ and 5% Fe-$W_{18}O_{49}$, EPR spectra, and Nyquist plots of EIS) is available in the online version of this article at https://doi.org/10.26599/NR.2025.94907807.

## Data availability

All data needed to support the conclusions in the paper are presented in the manuscript and the Electronic Supplementary Material. Additional data related to this paper may be requested from the corresponding author upon request.

## Acknowledgements

This work was supported by the National Key Laboratory on Electromagnetic Environmental Effects (No. 6142205240402), the National Natural Science Foundation of China (No. 52103223), the Natural Science Foundation of Heilongjiang Province of China (No. YQ2023E027), the Fundamental Research Funds for the Central Universities (Nos. 3072024GH2605, 3072024XX2613, and 3072024XX2616), and Young Talent of Lifting engineering for Science and Technology in Shandong, China (No. SDAST2025QTB019) for supporting this research. At the same time, we thank the Shandong Natural Science Foundation (Nos. ZR2024MA011 and ZR2023QA049) for their support in the theoretical calculation of this work.

## Declaration of competing interest

All the contributing authors report no conflict of interests in this work.

## Author contribution statement

X. H. S.: Conceptualization, experimental design, data curation, writing manuscript. W. W.: Investigation, experimental design. X. Y. Z.: Investigation, formal analysis. Z. Z. Q.: Methodology, experimental design. X. K.: Project administration, funding acquisition, theoretical calculation, writing and editing. X. Y. Z.: Project administration, funding acquisition. B. W.: Project administration, funding acquisition. X. H. R.: Resources, project administration. X. W. W.: Resources, project administration, funding acquisition. G. H. W.: Supervision, funding acquisition. N. N. L.: Supervision, project administration, funding acquisition, writing – review & editing. All the authors have approved the final manuscript.

## Use of AI statement

None.

## References

[1] Huang, R. N.; Xie, Y. F.; Cao, N. Z.; Jia, X. T.; Chao, D. M. Self-powered electrochromic smart window helps net-zero energy buildings. *Nano Energy* **2024**, *129*, 109989.

[2] Shao, Z. W.; Huang, A. B.; Cao, C. C.; Ji, X. W.; Hu, W.; Luo, H. J.; Bell, J.; Jin, P.; Yang, R. G.; Cao, X. Tri-band electrochromic smart window for energy savings in buildings. *Nat. Sustain.* **2024**, *7*, 796–803.

[3] Huang, S. C.; Guo, H. T.; Xia, P. F.; Sun, H. C.; Lu, C. G.; Feng, Y. G.; Zhu, J.; Liang, C.; Xu, S. H.; Wang, C. L. Integrated device of luminescent solar concentrators and electrochromic supercapacitors for self-powered smart window and display. *Nat. Commun.* **2025**, *16*, 2085.

[4] Li, S. L.; Chen, Y. Y.; Wang, Z.; Wang, M. M.; Guo, X. L.; Tang, X. Q.; Wang, X. Y.; Lai, W. D.; Tong, M. Y.; Wang, C. H. et al. Electrochromism via reversible electrodeposition of solid iodine. *Nat. Commun.* **2025**, *16*, 724.

[5] Huang, Y.; Wu, S. D.; Zhao, S. M.; Guo, Z. Y.; Zhao, Z. J.; Wu, X. K.; Wang, B. S.; Wang, F.; Xi, A. K.; Fan, L. et al. A novel liquid flow electrochromic smart window for all-year-round dynamic photothermal regulation. *Energy Environ. Sci.* **2025**, *18*, 1824–1834.

[6] Zhang, S.; Han, X.; Liu, X. C.; Huang, Z. X.; Wang, P. Y.; Sheng, S. Z.; Wu, G.; He, J. C.; Guo, J. J.; Zheng, X. S. et al. Amorphous-crystalline interface induced internal electric fields for electrochromic smart window. *Adv. Mater.* **2024**, *36*, 2410355.

[7] Riganti, M.; Castri, G. L.; Serra, V.; Manca, M.; Favoino, F. Energy saving potential of advanced dual-band electrochromic smart windows for office integration. *Energy Build.* **2025**, *327*, 115084.

[8] Zhao, F. F.; Wang, B.; Huang, B. K.; Zhang, W.; Chen, J. W.; Liu, L. H.; Wang, H. Z.; Elezzabi, A. Y.; Lee, P. S.; Milliron, D. J. et al. Inorganic electrochromic smart windows for advancing building energy efficiency. *Nat. Rev. Clean Technol.* **2025**, *4*, 396–412.

[9] Zhao, S. M.; Wang, B. S.; Zhu, N.; Huang, Y.; Wang, F.; Li, R.; Zhao,

Y. L.; Jiang, Q. Y.; Wu, X. K.; Zhang, R. F. Dual-band electrochromic materials for energy-saving smart windows. *Carbon Neutralization* **2023**, *2*, 4–27.

[10] Zhai, Y. L.; Li, J. H.; Shen, S.; Zhu, Z. J.; Mao, S.; Xiao, X.; Zhu, C. Z.; Tang, J. G.; Lu, X. Q.; Chen, J. Recent advances on dual-band electrochromic materials and devices. *Adv. Funct. Mater.* **2022**, *32*, 2109848.

[11] Huang, Z. K.; Peng, Y. T.; Zhao, J.; Zhang, S. L.; Qi, P. L.; Qu, X. L.; Yan, F. Q.; Ding, B.; Xuan, Y. M.; Zhang, X. G. An efficient and flexible bifunctional dual-band electrochromic device integrating with energy storage. *Nano-Micro Lett.* **2025**, *17*, 98.

[12] Bai, T.; Li, W. Z.; Fu, G. X.; Zhang, Q. Q.; Zhou, K. L.; Wang, H. Dual-band electrochromic smart windows towards building energy conservation. *Solar Energy Mater. Solar Cells* **2023**, *256*, 112320.

[13] Wang, J. K.; Wang, Z. P.; Zhang, M.; Huo, X. T.; Guo, M. Toward next-generation smart windows: An in-depth analysis of dual-band electrochromic materials and devices. *Adv. Opt. Mater.* **2024**, *12*, 2302344.

[14] Llordés, A.; Garcia, G.; Gazquez, J.; Milliron, D. J. Tunable near-infrared and visible-light transmittance in nanocrystal-in-glass composites. *Nature* **2013**, *500*, 323–326.

[15] Kim, J.; Ong, G. K.; Wang, Y.; LeBlanc, G.; Williams, T. E.; Mattox, T. M.; Helms, B. A.; Milliron, D. J. Nanocomposite architecture for rapid, spectrally-selective electrochromic modulation of solar transmittance. *Nano Lett.* **2015**, *15*, 5574–5579.

[16] Huang, Y.; Wang, B. S.; Bai, X. J.; Han, Y.; Zhang, W. S.; Zhou, C. H.; Meng, H. B.; Chen, F. X.; Wu, X. K.; Jiang, Q. Y. et al. 3D pine-needle-like $W_{18}O_{49}/TiO_2$ heterostructures as dual-band electrochromic materials with ultrafast response and excellent stability. *Adv. Opt. Mater.* **2022**, *10*, 2102399.

[17] Amate, R. U.; Morankar, P. J.; Teli, A. M.; Beknalkar, S. A.; Jeon, C. W. Synergistic design of processable $Nb_2O_5$–$TiO_2$ bilayer nanoarchitectonics: Enabling high coloration efficiency and superior stability in dual-band electrochromic energy storage. *J. Colloid Interface Sci.* **2025**, *678*, 431–445.

[18] Wang, K.; Meng, Q. C.; Wang, Q. K.; Zhang, W.; Guo, J. Q.; Cao, S.; Elezzabi, A. Y.; Yu, W. W.; Liu, L. H.; Li, H. Z. Advances in energy-efficient plasmonic electrochromic smart windows based on metal oxide nanocrystals. *Adv. Energy Sustain. Res.* **2021**, *2*, 2100117.

[19] Qin, L. X.; Liu, Y. W.; Long, M.; Zou, B. S.; Cao, S. Advancements in dual-band electrochromic smart windows: Exploring single-component materials for sustainable building solutions. *Ceram. Int.* **2024**, *50*, 22174–22183.

[20] Cao, S.; Zhang, S. L.; Zhang, T. R.; Yao, Q. F.; Lee, J. Y. A visible light-near-infrared dual-band smart window with internal energy storage. *Joule* **2019**, *3*, 1152–1162.

[21] Barawi, M.; De Trizio, L.; Giannuzzi, R.; Veramonti, G.; Manna, L.; Manca, M. Dual band electrochromic devices based on Nb-doped $TiO_2$ nanocrystalline electrodes. *ACS Nano* **2017**, *11*, 3576–3584.

[22] Zhang, S. L.; Cao, S.; Zhang, T. R.; Lee, J. Y. Plasmonic oxygen-deficient $TiO_{2-x}$ nanocrystals for dual-band electrochromic smart windows with efficient energy recycling. *Adv. Mater.* **2020**, *32*, 2004686.

[23] Zydlewski, B. Z.; Milliron, D. J. Dual-band electrochromic devices utilizing niobium oxide nanocrystals. *ACS Appl. Mater. Interfaces* **2024**, *16*, 24920–24928.

[24] Liang, Y.; Cao, S.; Guo, J. Q.; Zeng, R. S.; Zhao, J. L.; Zou, B. S. Dual-band electrochromic smart window based on single-component nanocrystals. *ACS Appl. Electron. Mater.* **2022**, *4*, 5109–5118.

[25] Liu, R.; Li, Y. Y.; Hu, B.; Long, Y. Organic ligand-free scalable dual-band electrochromic smart windows. *Adv. Funct. Mater.* **2025**, *35*, 2409914.

[26] Zheng, J. Y.; Sun, Q. M.; Cui, J. M. Z.; Yu, X. M.; Li, S. J.; Zhang, L. L.; Jiang, S. Y.; Ma, W.; Ma, R. Z. Review on recent progress in $WO_3$-based electrochromic films: Preparation methods and performance enhancement strategies. *Nanoscale* **2023**, *15*, 63–79.

[27] Chen, M. J.; Deng, J. B.; Zhang, H. L.; Zhang, X.; Yan, D. K.; Yao, G. X.; Hu, L. P.; Sun, S. K.; Zhao, J. P.; Li, Y. Advanced dual-band smart windows: Inorganic all-solid-state electrochromic devices for selective visible and near-infrared modulation. *Adv. Funct. Mater.* **2025**, *35*, 2413659.

[28] Wang, J. K.; Wang, Z. P.; Cui, L. X.; Zhang, M.; Huo, X. T.; Guo, M. Visible-near infrared independent modulation of hexagonal $WO_3$ induced by ionic insertion sequence and cavity characteristics. *Adv. Mater.* **2024**, *36*, 2406939.

[29] Hou, F. M.; Wei, W.; Yang, J.; Zhang, X. K.; Li, Z. Y.; Wei, A. *In situ* carbothermal reduction of oxygen vacancies in monoclinic $WO_{3-x}$ film for dual-band electrochromic windows. *Ceram. Int.* **2024**, *50*, 33400–33408.

[30] Meng, Q. C.; Cao, S.; Guo, J. Q.; Wang, Q. K.; Wang, K.; Yang, T.; Zeng, R. S.; Zhao, J. L.; Zou, B. S. Sol–gel-based porous Ti-doped tungsten oxide films for high-performance dual-band electrochromic smart windows. *J. Energy Chem.* **2023**, *77*, 137–143.

[31] Wang, Z. Q.; Guo, X. D.; Ma, F. H.; Wang, H. Y.; Zhang, C. H.; Xu, J. L.; Hu, R. M.; Cai, G. F.; Jiang, X. C. Heteroatom co-doping engineering endows tungsten oxide with highly efficient dual-band electrochromic performance. *Chem. Eng. J.* **2025**, *509*, 161281.

[32] Yan, N. F.; Cui, H. M.; Shi, J. S.; You, S. Y.; Liu, S. Recent progress of $W_{18}O_{49}$ nanowires for energy conversion and storage. *Tungsten* **2023**, *5*, 371–390.

[33] Pattathil, P.; Scarfiello, R.; Giannuzzi, R.; Veramonti, G.; Sibillano, T.; Qualtieri, A.; Giannini, C.; Cozzoli, P. D.; Manca, M. Near-infrared selective dynamic windows controlled by charge transfer impedance at the counter electrode. *Nanoscale* **2016**, *8*, 20056–20065.

[34] Huang, Y.; Wang, B. S.; Lyu, P.; Zhao, S. M.; Wu, X. K.; Zhang, S. L.; Li, R.; Jiang, Q. Y.; Wang, F.; Zhao, Y. L. et al. Oxygen-deficient tungsten oxide nanoflowers for dynamically tunable near-infrared light transmittance of smart windows. *Nano Res.* **2023**, *16*, 12165–12172.

[35] Sun, X. H.; Wu, W.; Liu, N. N.; Li, P.; Zhao, X. Y.; Qu, Z. Z.; Zhao, K. M.; Wang, B.; Rong, X. H.; Zhang, X. Y. et al. Controlled assembly and synthesis of oxygen-deficient $W_{18}O_{49}$ films based on solvent molecular strategy for electrochromic energy storage smart windows. *Chem. Eng. J.* **2024**, *499*, 156109.

[36] Wang, W. G.; Tian, B. Q.; Yang, X. N.; Zhu, S.; Jian, M. L.; Yang, L. Q. Significantly enhanced oxygen vacancies in $W_{18}O_{49}$ nanowires for electrochromic films by annealing in argon. *Ceram. Int.* **2024**, *50*, 19898–19909.

[37] Cai, X. S.; Xiao, X. D.; Sheng, G. Z.; Zheng, J. Y.; Zhao, Y. J.; Xu, G. Effect of pH on the structure and morphology of $W_{18}O_{49}$ nanowires and their electrochromic properties. *Ceram. Int.* **2022**, *48*, 20791–20800.

[38] Hassan, M.; Li, P. P.; Lin, J.; Li, Z. H.; Javed, M. S.; Peng, Z. C.; Celebi, K. Smart energy storage: $W_{18}O_{49}$ NW/$Ti_3C_2T_x$ composite-enabled all solid state flexible electrochromic supercapacitors. *Small* **2024**, *20*, 2400278.

[39] Fu, B.; Qu, X. S.; Song, Y. Y.; Li, F. R.; Shi, H. W.; Lv, Y. X.; Wang, J. L.; Jin, H.; Yu, X. Y.; Yang, Y. Y. Polyoxotungstate/$W_{18}O_{49}$ nanocomposite with a bird-nest-like network supports high-performance electrochromic supercapacitors. *Nanoscale* **2025**, *17*, 6103–6114.

[40] Xie, Y.; Huang, R.; Li, M.; Cao, N.; Jia, X.; Wang, C.; Chao, D. Reusing the wasted energy of electrochromic smart window for near-zero energy building. *Adv. Sci.* **2024**, *11*, 2406232.

[41] Zhao, F. F.; Wang, B.; Zhang, W.; Cao, S.; Liu, L. H.; Elezzabi, A. Y.; Li, H. Z.; Yu, W. W. Counterbalancing the interplay between electrochromism and energy storage for efficient electrochromic devices. *Mater. Today* **2023**, *66*, 431–447.

[42] Kresse, G.; Furthmüller, J. Efficient iterative schemes for *ab initio* total-energy calculations using a plane-wave basis set. *Phys. Rev. B* **1996**, *54*, 11169–11186.
[43] Kresse, G.; Joubert, D. From ultrasoft pseudopotentials to the projector augmented-wave method. *Phys. Rev. B* **1999**, *59*, 1758–1775.
[44] Perdew, J. P.; Burke, K.; Ernzerhof, M. Generalized gradient approximation made simple. *Phys. Rev. Lett.* **1996**, *77*, 3865–3868.
[45] Blöchl, P. E. Projector augmented-wave method. *Phys. Rev. B* **1994**, *50*, 17953–17979.
[46] Xu, K.; Xu, Z. F.; Wang, L.; Feng, H. F.; Pan, F.; Zhuang, J. C.; Du, Y.; Hao, W. C. First-principles study on the electronic structures and diffusion behaviors of intrinsic defects in BiOCl. *Comput. Mater. Sci.* **2022**, *203*, 111088.
[47] Wu, Z. S.; Lian, Z. D.; Ding, T.; Li, J. L.; Xu, J. C.; Wang, J. X.; Zhang, L. X.; Wang, B.; Chen, S.; Xiao, P. et al. Inhibiting the phase transition of $WO_3$ for highly stable aqueous electrochromic battery. *J. Energy Chem.* **2024**, *95*, 86–95.
[48] Park, S.; Park, H. S.; Dao, T. T.; Song, S. H.; Lee, S. I.; Van Tran, H.; Ullah, A.; Han, C. H.; Hong, S. J. Solvothermal synthesis of oxygen deficient tungsten oxide nano-particle for dual band electrochromic devices. *Solar Energy Mater. Solar Cells* **2022**, *242*, 111759.
[49] Sun, X. H.; Wang, D.; Wu, W.; Zhao, X. Y.; Zhang, X. Y.; Wang, B.; Rong, X. H.; Wu, G. H.; Wang, X. W. Amorphous and crystalline Ti-doped $WO_3{\cdot}2H_2O$ for dual-band electrochromic smart windows. *ACS Sustain. Chem. Eng.* **2024**, *12*, 5459–5467.
[50] Qu, Z. Z.; Li, A. K.; Gao, M.; Sun, X. H.; Zhang, X. Y.; Wu, G. H.; Wang, X. W. Effect of Co-doping on the electrochromic performance of hexagonal phase $WO_3$ nanorods. *Dalton Trans.* **2024**, *53*, 17221–17232.
[51] Zhuang, D. S.; Zhang, Z. X.; Weng, J. B.; Wang, J. Y.; Zhang, H. L.; Cheng, W. Amorphous hydrated tungsten oxides with enhanced pseudocapacitive contribution for aqueous zinc-ion electrochromic energy storage. *Adv. Energy Mater.* **2024**, *14*, 2402603.
[52] Chen, N. K.; Wang, B. Q.; Niu, M.; Sun, H. B.; Zhang, S. B.; Li, X. B. Intensive structural disorder induces electronic delocalization: Amorphous solid–liquid transition in ovonic threshold switching materials. *Adv. Funct. Mater.* **2024**, *34*, 2410622.
[53] Sun, X. H.; Li, Q. G.; Liu, N. N.; Wang, B.; Zhang, X. Y.; Qian, H. N.; Lv, Y. S.; Rong, X. H.; Wu, G. H.; Wang, X. W. Interface engineering of $SnO_2$ to enhance the cycle stability of $WO_3$ and Prussian blue for complementary electrochromic smart windows and energy storage. *Ceram. Int.* **2024**, *50*, 33630–33637.
[54] Fu, X. F.; Li, K.; Zhang, C. L.; Wang, Q.; Xu, G. L.; Rogachev, A. A.; Yarmolenko, M. A.; Cao, H. T.; Zhang, H. L. Homogeneous and nanogranular prussian blue to enable long-term-stable electrochromic devices. *ACS Appl. Mater. Interfaces* **2024**, *16*, 17745–17756.